https://doi.org/10.26599/FRICT.2026.9441331

Research Article

Phase-field analysis on the interfacial damage behavior of high-speed bearings under impact-sliding conditions

Weiwei Man[a,b], Liqin Wang[a,c], Panlong Wu[a,c], Wanjia Li[a,c*], Zongxiang Yue[a,c], Jinbao Huang[a,c], Tingjian Wang[a,c*], Le Gu[a,c], and Chuanwei Zhang[a,c]

[a] *School of Mechatronics Engineering, Harbin Institute of Technology, Harbin 150001, China*

[b] *AECC Hunan Aviation Powerplant Research Institute, Zhuzhou 412000, China*

[c] *Zhengzhou Advanced Research Institute, Harbin Institute of Technology, Zhengzhou 450000, China*

* Corresponding author： Wanjia Li, E-mail: wanjia@hit.edu.cn

Tingjian Wang, E-mail: wangtj@hit.edu.cn

Received: July 9, 2026; Revised: October 24, 2026; Accepted: October 29, 2026

© The Author(s) 2026.

Just Accepted

Abstract

Transient impact-sliding contacts between the cage and the guiding ring under starved lubrication severely threaten the structural reliability of high-speed aero-engine main bearings. Traditional analytical and implicit finite element methods struggle to capture the highly nonlinear competitive failure mechanisms at this dual-body interface due to severe convergence bottlenecks and non-realistic single-body simplifications. In this study, a novel, fully coupled thermo-elasto-plastic phase-field fracture framework is proposed to systematically investigate the asymmetric damage evolution between an M50 steel ring and an AISI 4340 steel cage. The simulation results reveal a profound synergistic coupling effect between the normal impact and tangential sliding velocities. Furthermore, a fundamental disparity in spatial damage morphology is observed: the high-hardness M50 ring exhibits surface-initiated, elastic-dominated incipient micro-damage localization, whereas the tougher 4340 cage accommodates kinetic energy through subsurface-initiated, volumetric, thermo-elasto-plastic flow. Crucially, an asymmetric competitive degradation mechanism governed by an interfacial thermal partition coefficient is uncovered. By purposefully channeling a substantial fraction of the frictional heat into the 4340 cage, the cage undergoes catastrophic thermal softening and massive yielding, autonomously acting as a thermodynamic sacrificial buffer. This mechanism dynamically absorbs the destructive impact energy, physically shielding the core M50 ring from severe fatigue fracture. The extracted damage transition phase diagram provides a robust, physics-based criterion for the advanced surface engineering and thermal management of aerospace bearings.

Keywords: M50 steel; impact-sliding; thermal partition; damage; phase-field

Just Accepted

1. Introduction

The main bearing in an aeroengine is a crucial component of its rotating system, and its reliability directly affects the aircraft's safety. M50 steel is widely used for aero-engine main bearing rings due to its excellent high-temperature mechanical properties [1,2]. Meanwhile, bearing cages are typically fabricated from 4340 steel, a high-strength, quenched-and-tempered alloy steel [3,4]. This material is selected for its exceptionally high yield strength, superior ductility, and outstanding overall fracture toughness [5–7]. Therefore, it is a typical and common combination of M50 steel ring and 4340 steel cage in an aero-engine main bearing. As the aero-engine's dynamic limit increases, the serving conditions of bearing become extremely harsh, and the occurrence frequency of high-rotating speed and starved lubrication is increasing. As aero-engines push toward higher dynamic thresholds, their main bearings are subjected to increasingly harsh environments, in which transient ultra-high speeds and severe oil starvation occur more frequently. Such rigorous conditions accelerate surface degradation at the cage-ring contact interface, profoundly compromising overall bearing reliability [8–10]. Therefore, it is crucial to elucidate the mechanism of the surface damage formation and proposed predictive methodology.

The interaction status between the cage and ring in a running bearing is the primary task to be confirmed. Researchers established dynamic models and studied the interactions among the components of a rolling bearing, including the roller, ring, and cage, during operation, and found collisions between the cage and ring under special conditions [10–14]. Once the bearing's rotational speed fluctuates drastically or is subjected to external aerodynamic excitation, the cage's motion stability will be lost [11,12]. This cage instability leads to a complex contact status called impact-sliding [14,15]. Impact-sliding is a detrimental status to the contact surface compared to pure rolling and sliding. The impact load will break the elastohydrodynamic lubrication (EHL) film and induce tremendous frictional heat and localized tangential shear stress between the cage and the ring [16].

Just Accepted

This causes the contact interface to experience high frictional heat and shear stress, accelerating surface thermal softening and damage formation [17]. Extensive research has been conducted to study the behavior of surface damage under impact and sliding contact conditions. Wu and Peter et al. [18,19] proposed an impact theory for a sphere-plate contact pair to calculate the dynamic contact time, pressure, and energy dissipation. Li and Gheadnia et al. [20,21] analyzed the obliquity angle effects on the plastic deformation by performing theoretical and experimental analysis for the elasto-plastic oblique impact for a rod and flat contact pair. Damabakizi et al. [22,23] established a multiscale thermomechanical modeling to analyze the thermos-mechanical behavior, including friction and plastic work, thermal softening, and melting. These studies share the idea of using oblique contact to simulate the impact-slide process. For the impact-slide on a plate, where the oblique contact angle is zero, Zhang et al. [24,25] analyzed the stress distribution and plastic deformation, considering thermal asperity effects, for the contact pair between sensors and the disk without oblique contact. Although these studies have illuminated the tribological mechanism underlying impact-sliding contact behavior, the assessment of surface bearing capacity after contact-sliding loading is ignored.

The surface bearing capacity assessment quantifies the degree of stiffness degradation, always indicated by a damage factor. In computational solid mechanics, continuum damage mechanics (CDM) is widely used to quantify this degradation by coupling the macroscopic damage factor to the constitutive equations [24,25]. In CDM, damage is a factor ranging from 0 to 1 that indicates the degree of degradation. There are various models for the damage evolution of steels under different loading conditions and failure mechanisms. For instance, the Lemaitre model represents a thermodynamically consistent isotropic CDM approach, utilizing the strain-energy equivalence principle to simulate continuous macroscopic stiffness degradation [24]. The Gurson model is a micromechanics-based approach that describes ductile fracture [26]. The Johnson-Cook model is a phenomenological criterion specifically formulated for high-strain-rate and elevated-temperature

Just Accepted

environments [27]. Additionally, the Bao-Wierzbicki model extends ductile failure predictions by incorporating the Lode angle parameter alongside stress triaxiality, thereby accurately characterizing fracture behavior under complex stress states such as shear, tension, and compression [28]. Furthermore, Energy-based damage models rely on critical strain energy density or specific fracture dissipation energy as the indicator of element failure [29]. Although these damage evolution criteria can satisfy most serving conditions for most steels, they are difficult to apply to impact-sliding contact conditions, especially for the serving conditions of area-engine bearings at extremely high revolving speeds. Impact-sliding contact conditions significantly increase the difficulty of solving the numerical models. Therefore, researchers make attempts to simplify the impact-sliding contact conditions. Zhang et al. [32] proposed a semi-analytical method and used the Fourier transform method to study shear instability and severe plastic flow under rolling-sliding contact conditions in M50 bearing steel. However, their model decouples thermal history from dynamic deformation and cannot describe the continuous damage and real-time dual-body interactions. Then, the finite element method has been applied to investigate the coupled deformation and thermal responses. Wang et al. [15] evaluated the surface damage of M50 steel under impact-sliding contact conditions, considering thermal effects. However, their study employs moving loads and idealized heat sources on the contact surfaces rather than a real cage to ensure computational feasibility. This decoupled approach inherently neglects real-time dynamic heat partitioning and mutual structural degradation. To more effectively characterize complex continuous damage evolution and fracture behavior, advanced numerical techniques such as the phase-field method have been increasingly adopted in computational mechanics. They can predict crack nucleation, propagation, and complex topology changes driven by thermodynamic energy minimization [30]. The phase-field method was also adopted by Wang et al. [31] to investigate near-surface damage accumulation under impact-sliding conditions. However, their formulation relied on idealized moving loads rather than an explicit cage geometry. Consequently, the competitive damage evolution and asymmetric energy dissipation between the softer cage and the high-hardness ring

Just Accepted

remain unexplored under coupled thermomechanical conditions. Furthermore, standard implicit User Element (UEL) subroutines exhibit severe convergence bottlenecks under extreme high-speed impact-sliding dynamics. To overcome these limitations, a fully coupled dynamic framework incorporating real cage-ring contact interactions is urgently required.

In this study, the authors established a novel dynamic model to analyze surface damage under impact-sliding contact on both the cage and ring surfaces. The proposed model is based on explicit Vectorized User Element (VUEL) subroutines and is coupled with thermos softening, damage degradation, heat generation from deformation and friction, and contact heat conduction. The effects of impact and sliding velocity, friction coefficients, and thermodynamic partition coefficient on the surface damage of the M50 steel ring and the 4340 steel cage were investigated. The organization of this study is as follows. Firstly, the unified thermo-elasto-plastic constitutive equations and phase-field fracture mechanics were described in the numerical method section. Secondly, a dual-body FEM model, including the cage and ring, employing a multi-layer element architecture was established to calculate the transient damage evolution. Thirdly, the dynamic thermo-mechanical responses, competitive energy dissipation trajectories, and spatial damage morphologies under various kinematic and frictional parameters were obtained. Finally, the synergistic impact-sliding effects and the competitive degradation mechanism were discussed, and the numerical model was validated.

2. Numerical Method

This study uses a coupled thermo-mechanical dynamics model to describe the mechanical responses, thermal softening, and damage evolution of both the ring and cage. The proposed model was developed in Fortran as the VUEL subroutine implemented in Abaqus. The FEM model of the impact-sliding contact pair is established using the preprocessing tools in Abaqus and a self-developed MATLAB script to modify the input file. In the Abaqus input file, the custom 4-node

Just Accepted

explicit user elements were defined. To accurately capture the multi-physics coupling mechanisms, the active nodal degrees of freedom (DOFs) are specifically mapped to govern the spatial displacements, the thermal field, and the phase-field fracture evolution. To realize contact between the real ring and cage and to perform post-processing in ABAQUS, dummy elements with negligibly low stiffness were introduced. As shown in Fig. 1, the 1st layer is the core element, with the VUEL subroutine serving as the computational engine, receiving these boundary load inputs to simultaneously execute the underlying thermo-mechanical coupled integration and phase-field damage evolution. The 2nd layer is established only at the contact area. It is used to simulate surface interactions and to directly transfer real-time contact stresses and frictional heat to the primary VUEL elements. The 3rd layer is established to overcome the inherent limitation that custom user elements cannot directly output result contours. The VUEL continuously transfers its internally updated solution-dependent state variables (SDVs) to the VUSDFLD subroutine in real time. Through this variable transfer method, complex internal physical fields are successfully mapped back onto the dummy elements, thereby enabling intuitive and highly accurate post-processing contour visualizations within the Abaqus platform.

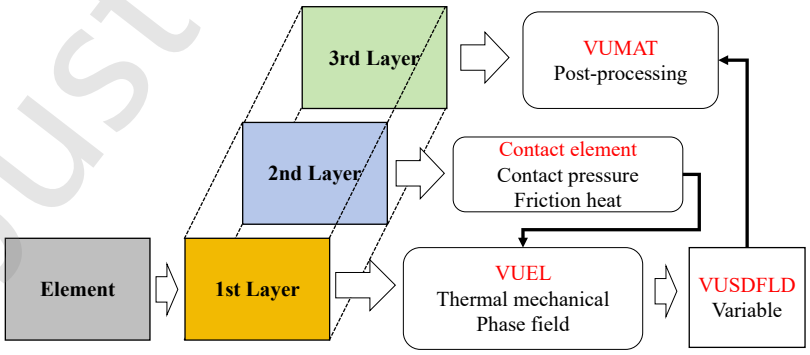


Fig. 1. Schematic of the custom element VUEL computational layer (contact layer, and VUSDFLD visualization layer).

2.1 Thermo-elasto-plastic constitutive model

Just Accepted

The impact-sliding contact is a complex loading condition that induces thermal softening and plastic deformation. Therefore, this study uses the thermo-elasto-plastic theory to describe the stress and strain behavior. The thermo-elasto-plastic theory assumes that the strain is within a small range, and divides the total strain tensor into elastic, plastic, and thermal components as follows:

$$\boldsymbol{\varepsilon} = \boldsymbol{\varepsilon}^e + \boldsymbol{\varepsilon}^p + \boldsymbol{\varepsilon}^{th} \tag{1}$$

where $\boldsymbol{\varepsilon}^e$ is the elastic strain tensor, $\boldsymbol{\varepsilon}^p$ is the plastic strain tensor, $\boldsymbol{\varepsilon}^{th}$ is the thermal tensor, which is proportional to the temperature increment, $\boldsymbol{\varepsilon}^{th} = \alpha_{th}\dot{\theta}\mathbf{I}$. Herein, α_{th} is the thermal expansion coefficient varies with temperature, $\dot{\theta}$ is the temperature increment, $\mathbf{I}$ is the identity tensor.

According to the CDM theory and generalized Hooke's law, the Cauchy stress tensor after damaged is evaluated by the following equation as:

$$\sigma = g(d)\mathbb{C}_{th}:\left(\varepsilon - \varepsilon^p - \varepsilon^{th}\right) \tag{2}$$

$$g(d) = (1-d)^2 \tag{3}$$

where $\mathbb{C}_{th}$ is the temperature-dependent elastic stiffness tensor, $g(d)$ is the degradation function, d is the damage factor.

In this study, J_2 von Mises yield criterion coupled with a nonlinear isotropic hardening rule is selected, shown as follows:

$$F_y = \sqrt{\frac{3}{2}\mathbf{S}:\mathbf{S}} - \sigma_y - R \text{ with } \mathbf{S} := \mathrm{dev}[\boldsymbol{\sigma}] \tag{4}$$

where $\mathbf{S}$ is the effective stress tensor, σ_y is the yield strength, and R is the isotropic hardening stress from the thermal expansion. The yield strength in this study is depth- and thermally dependent. A Logistic evolution model based on the Fermi-Dirac distribution is used in this study. This model can accurately capture the catastrophic strength collapse of high-strength steels under extreme heating,

Just Accepted

compared with the traditional phenomenological power-law model [32], and the depth-dependent describes the gradient distribution of the hardness [33]. Therefore, σ_y in this study is calculated as follows:

$$\sigma_y = \sigma_{y_0} S_{th}(T,h) S_{\text{depth}}(h) \tag{5}$$

$$S_{th}(T,h) = \left[1 + \exp\left(\omega_1\left(T_{abs} - T_{ref}(h)\right)\right)\right]^{-1} \tag{6}$$

$$S_{\text{depth}}(h) = \exp\left(-a_1 h - a_2 h^2\right) \tag{7}$$

where σ_{y_0} is the original yield strength at the room temperature, ω_1 is the softening rate, T_{abs} is the absolute temperature, $T_{ref}(h)$ is the depth-dependent reference transition temperature, h is the distance from the surface, a_1 and a_2 are the fitting parameters.

Once the stress exceeds the yielding strength, the plastic strain tensor $\boldsymbol{\varepsilon}^p$ is determined by the following plastic flow rule as,

$$\dot{\boldsymbol{\varepsilon}}^p = \dot{p}\frac{\partial F}{\partial \tilde{\boldsymbol{\sigma}}} = \frac{3}{2}\dot{p}\frac{\tilde{\mathbf{s}}}{\tilde{\sigma}_{eq}} \tag{8}$$

where $\dot{p}$ is the equivalent plastic strain rate, $\dot{p} = \sqrt{2(\dot{\boldsymbol{\varepsilon}}^p : \dot{\boldsymbol{\varepsilon}}^p)/3}$, $\tilde{\mathbf{s}}$ is the effective deviatoric stress tensor, $\tilde{\sigma}_{eq}$ is the effective equivalent stress.

2.2 Phase-field model coupled with thermo-elasto-plastic model

According to the isotropic constitutive model, this study considers the isotropic solid domain Ω, characterized by the displacement field $\mathbf{u}(\mathbf{x},t)$, temperature field $\theta(\mathbf{x},t)$, and crack phase-field $\phi(\mathbf{x},t)$. The phase-field parameter $\phi \in [0,1]$ is used to define a crack surface functional Γ_l. At the initial state, ϕ is 0 indicate the material has no damage. Once ϕ reaches 1, it indicates the material is completely damaged, which means it has no stiffness. As shown in Fig. 2, the external boundary is

Just Accepted

partitioned into distinct regions, where the prescribed boundaries satisfy $\partial\Omega_{\mathrm{t}} \cup \partial\Omega_{\mathrm{u}} = \partial\Omega$ with $\partial\Omega_{\mathrm{t}} \cup \partial\Omega_{\mathrm{u}} = \phi$, and similarly for the thermal boundaries, $\partial\Omega_{\mathrm{J}} \cup \partial\Omega_{\theta} = \partial\Omega$ with $\partial\Omega_{\mathrm{J}} \cup \partial\Omega_{\theta} = \phi$. Herein, $\partial\Omega_{\mathrm{u}}$, $\partial\Omega_{\mathrm{t}}$, Ω_{θ}, and Ω_{J} indicate the displacement, traction, temperature, and heat flux boundary, respectively. The region γ represents a localized internal heat source. In Fig. 2(a), the Γ is the sharp crack at the limit $l_{\mathrm{c}} \to 0$. In Fig. 2(b), Γ_l is the regularized crack whose width is controlled by the length scale parameter l_{c}. Here, l_{c} acts as a critical characteristic dimension that regulates the spatial width of the diffuse damage zone, thereby transforming discrete sharp cracks into continuous smeared topologies and eliminating the pathological mesh dependence in numerical fracture simulations.

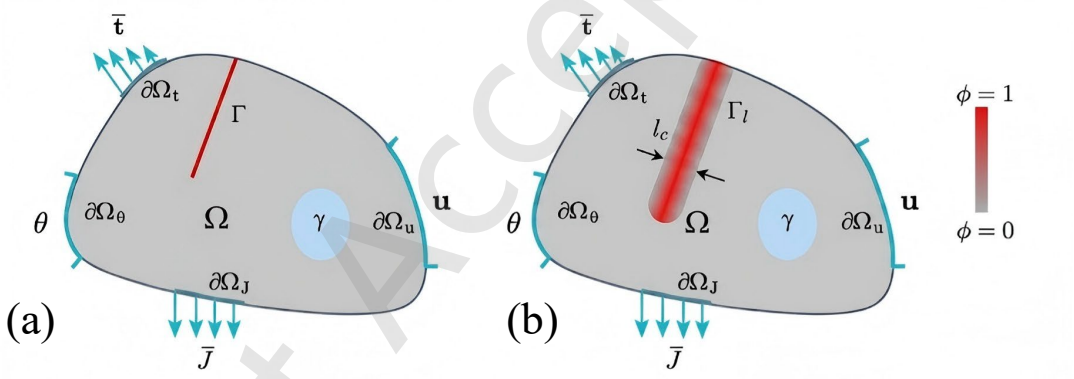


Fig. 2. Fractured domain Ω with crack surface. a) Sharp crack topology Γ; b) Regularized crack topology Γ_l.

Fracture thermodynamics divides the total potential energy function into stored deformation energy, stored thermal energy, and fracture dissipation energy associated with crack surface formation [34,35]. The total potential energy evolution is described as follows:

$$\Psi = \int_{\Omega} [\psi_{\mathrm{def}}(\varepsilon^e, p, \phi) + \psi_{\mathrm{thermal}}(\theta) + \mathcal{G}_c \gamma(\phi, \nabla\phi)] dV \tag{9}$$

$$\gamma(\phi, \nabla\phi) = \frac{1}{2l_c}\phi^2 + \frac{l_c}{2}|\nabla\phi|^2 \tag{10}$$

Just Accepted

where ψ_{def} is the free energy density from mechanical deformation, ψ_{thermal} is the thermal energy density, and $\mathcal{G}_c$ is the critical strain energy release rate, $\gamma(\phi, \nabla\phi)$ is the crack surface geometric density function, and l_c is the length scale parameter.

The stored deformation energy ψ_{def} is contributed by the elastic strain energy ψ_{e} and a fraction of the irreversible plastic dissipation ψ_{p}. The elastic strain energy is divided into a tensile part ψ_e^+ and the compression part ψ_e^-. As the compressive loads tend to close the micro-cracks rather than open them, and some plastic work is attributed to heat generation, researchers proposed the driving energy without considering the ψ_e^- and part of ψ_{p} [36,37]. The driving energy for the phase is defined as:

$$\psi_{\text{drive}} = \psi_e^+ + (1-\eta)\psi_{\text{p}} \tag{11}$$

where η is the Taylor-Quinney coefficient that defines the fraction of plastic work transformed into heat [38], ψ_{p} represents the total irreversible plastic work density accumulated during the deformation process. This total plastic work is thermodynamically partitioned into two distinct components. The coefficient η defines the fraction of the total plastic work dissipated as heat, which serves as the internal thermal source in the governing heat conduction equation. Conversely, the remaining fraction $(1-\eta)$ denotes the cold work. It is precisely this stored cold-work portion that acts as the mechanical driving force for phase-field damage evolution. Herein, ψ_{e} and ψ_{p}were assumed to be expressed as:

$$\psi_e = \psi_e^- + g(d\phi)\psi_e^+ \tag{12}$$

$$\psi_e^+ = (\frac{\lambda}{2} + \frac{\mu}{2})\langle \text{tr}\boldsymbol{\varepsilon}^e \rangle_+^2 + \mu \|\text{dev}\boldsymbol{\varepsilon}^e\|^2 \tag{13}$$

$$\psi_e^- = (\frac{\lambda}{2} + \frac{\mu}{2})\langle \text{tr}\boldsymbol{\varepsilon}^e \rangle_-^2 \tag{14}$$

$$\psi_{\text{p}} = \int_0^t \tilde{\sigma} : d\varepsilon^p \tag{15}$$

Just Accepted

where the Macaulay brackets $\langle x \rangle_{\pm} = \frac{(x \pm |x|)}{2}$ extract the positive and negative principal value, λ and μ are the Lamé constants.

The thermal energy density $\psi_{\text{thermal}}(\theta)$ is formulated as :

$$\psi_{\text{thermal}}(\theta) = \rho c \left[(\theta - \theta_0) - \theta \ln \left(\frac{\theta}{\theta_0} \right) \right] \tag{16}$$

where ρ is the material mass density, c is the specific heat capacity, and θ_0 is the initial temperature.

To satisfy the damaged part cannot heal after unloading, and the thermodynamic irreversibility condition, a history maximum energy field variable $\mathcal{H}$ is induced as:

$$\mathcal{H}(\mathbf{x}, t) = \max_{\tau \in [0,t]} \psi_{\text{drive}}(\mathbf{x}, \tau) \tag{17}$$

2.3 Governing model

Phase-field evolution follows the energy-minimization principle based on the variational approach. A multi-physics equation governs the coupled boundary value for the domain Ω. This study focuses on the high-speed impact and sliding-load conditions. It differs from conventional quasi-static implicit models. In this study, macroscopic momentum conservation is formulated as a transient dynamic wave propagation problem that incorporates material inertia. The expression equation is shown as follows:

$$\rho \ddot{\mathbf{u}} = \nabla \cdot \sigma + \mathbf{b} \qquad \text{in } \Omega \tag{18}$$

where $\ddot{\mathbf{u}}$ is the macroscopic acceleration value, and $\mathbf{b}$ is the external body force vector.

The heat conduction equation governs the evolution of the temperature field. The thermal energy is dynamically sourced from the external heat source and the elastoplastic dissipation via the Taylor-Quinney coefficient as :

Just Accepted

$$\rho c\dot{\theta} = \nabla \cdot (k(\phi)\nabla\theta) + \eta\sigma : \dot{e}^p + \gamma \quad \text{in } \Omega \tag{19}$$

$$k(\phi) = g(\phi)k_0 \tag{20}$$

where $\dot{\theta}$ is the temperature rate, $\nabla\theta$ is the temperature gradient, $k(\phi)$ is the thermal conductivity coefficient after damaged, k_0 is the original thermal conductivity coefficient, and γ represents the equivalent volumetric heat source derived from the localized interfacial frictional work. Applying the identical isotropic degradation function $g(\phi)$ to both mechanical stiffness and thermal conductivity is a common simplification in phase-field modeling. From a strictly physical perspective, while macroscopic open cracks eliminate local tensile stiffness, thermal conduction can persist across the faces of closed cracks under compressive loads. However, because the maximum phase-field damage simulated in the present transient single-collision event remains relatively low, this simplified thermal degradation assumption introduces negligible quantitative deviation. The fundamental competitive energy-partitioning mechanisms discussed in this work are predominantly governed by bulk thermoplastic yielding and unfractured matrix behavior, and remain robust to this thermal-degradation simplification.

Finally, the governing equation for the phase-field damage evolution is expressed as follows:

$$\mathcal{G}_c \left(\frac{\phi}{l_c} - l_c \nabla^2 \phi \right) = 2(1-\phi)\mathcal{H} \tag{21}$$

2.4 Explicit numerical implementation

The preceding section of this study describes the key theoretical equations. These equations were developed by the VUEL subroutines and solved in the ABAQUS/EXPLICIT environment. The phase-field damage variable ϕ is mapped to the nodal degree of freedom (DOF) 8. The transient temperature θ is mapped to the nodal DOF 11. These mapped DOFs were integrated at the element nodes. The mathematical core of the explicit implementation in this study is the assumption that

Just Accepted

phase-field damage evolution is a pseudo-dynamic wave propagation process. The explicit central-difference time integration algorithm requires strictly diagonal capacity matrices to avoid computationally prohibitive global matrix inversions. The element-level artificial phase-field mass matrix and the thermal capacity matrix are constructed utilizing the standard row-sum lumping technique. Therefore, the nodal phase-field accelerations are evaluated by solving the decoupled discrete system:

$$\ddot{\boldsymbol{\phi}}_{(t)} = \mathbf{M}_{\phi}^{-1}\left(\mathbf{F}_{ext,(t)}^{\phi} - \mathbf{F}_{int,(t)}^{\phi}\right) \tag{22}$$

Where $\ddot{\boldsymbol{\phi}}$ is the acceleration vector of the fictitious nodal phase-field variable, $\mathbf{F}_{ext,(t)}^{\phi}$ and $\mathbf{F}_{int,(t)}^{\phi}$ are the external and internal phase-field force vectors, respectively, and $\mathbf{M}_{\phi}$ is the artificial phase-field lumped mass matrix.

2.5 Finite element model

In this study, a 2D FEM model was established as shown in Fig. 3. Based on the geometric characteristics of the ring and cage in a rolling bearing, both the cage and the ring were simplified under plane-strain conditions. Since the dynamic impact-sliding interaction is highly localized, only partial segments of the cage and the ring were extracted for modeling. The localized contact area was meshed with highly refined elements of 12 nm size. The computational domain was discretized using a multi-layer element formulation, as shown in Fig. 1. The 1st and 3rd layers of the dummy elements used the custom 4-node explicit user element and the ABAQUS CPE4RT element with negligibly low stiffness, respectively. The 1st layer was used to capture the elasto-plasticity and phase-field fracture evolution. The 3rd layer consisted of standard ABAQUS CPE4RT coupled temperature-displacement elements, assigned an artificially reduced mechanical stiffness to enable robust resolution of transient heat conduction without introducing any non-physical structural reinforcement. The kinematic contact formulation governed the impact-sliding interface. The contact pair was

Just Accepted

defined by tangential behavior, normal behavior, and thermal conductance. The tangential behavior selected penalty friction formulation. Normal behavior selected hard contact. And thermal conductance is defined as a pressure-dependent parameter. The mechanical constraint formulation selected the kinematic contact method. The bottom of the ring was fixed. The initial impact velocity V_i and sliding velocity V_s were directly applied to all nodes of the cage segment to drive the dynamic contact process. The initial temperature was applied to all nodes as well.

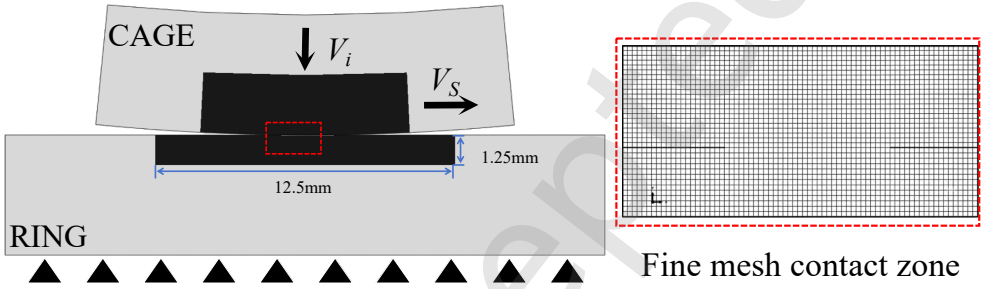


Fig. 3. Dual components Finite element model.

2.6 Material parameters

The ring and cage in aeroengine rolling bearings are the research targets in this study and were made from M50 and 4340 steels, respectively. The thermo-elasto-plastic constitutive model was introduced in the previous section. In this model, some crucial mechanical and thermal properties of the M50 and 4340 steels are temperature-dependent. Figure 4 shows the temperature-dependent material properties of the M50 and 4340 steels used in this study, and these parameters of M50 steel were obtained from Zhang et al. [15,33]. For the 4340 steel, the property parameters were comprehensively calibrated using multiple literature sources: Young's modulus and Poisson's ratio from Carnevale et al. [39], yield strength from Lee et al. [40], heat capacity and thermal conductivity from Fakir et al. [41], and the thermal expansion coefficient from Hussain et al. [42]. Material parameters of M50 and 4340 steels at ambient temperature (20 ℃) are listed in Table 1, with

Just Accepted

temperature-dependent properties up to 1000 °C plotted in Fig. 4. Above 1000 °C, each property is held at its last tabulated value. This extends the solid-state model beyond the available material data. Melting, latent heat of fusion, and the flow or removal of molten material are not included. Temperatures above the melting points in Table 1 cannot therefore be treated as predictions of the actual interface temperature. Stresses, plastic strain and phase-field damage calculated from these thermal histories are subject to the same limitation.

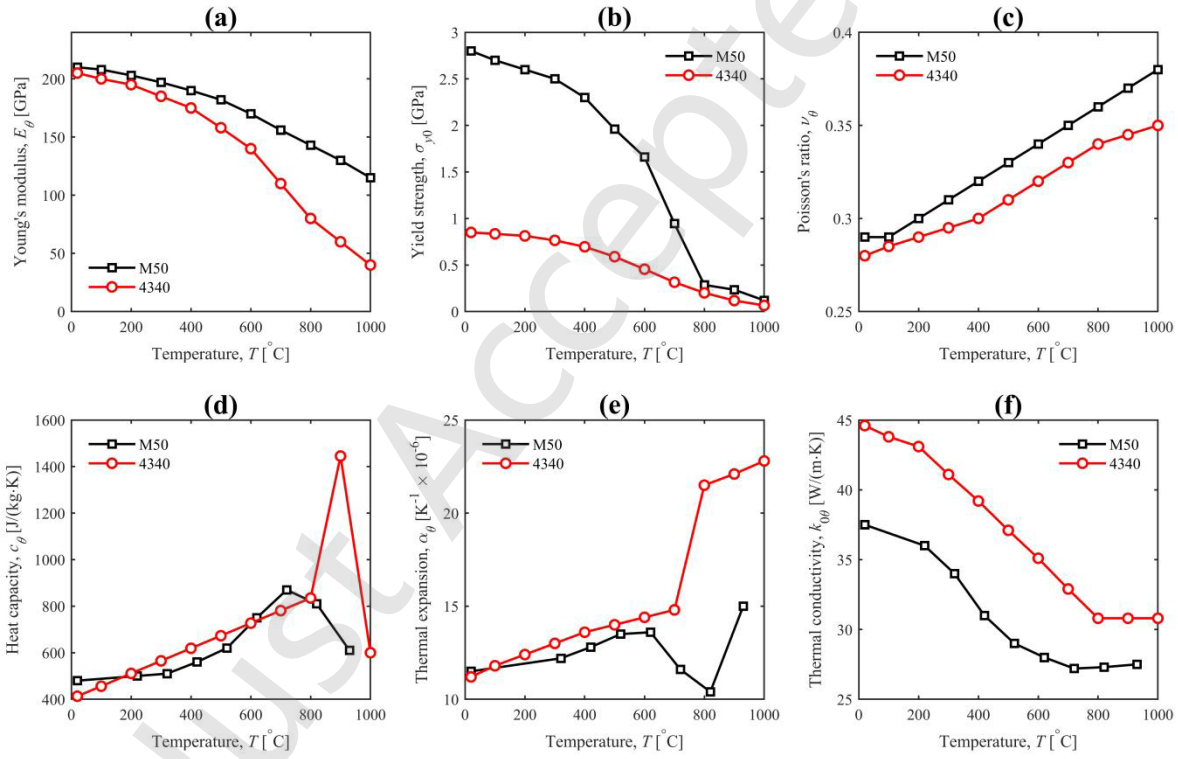


Fig. 4. Temperature-dependent material properties of M50 and 4340 steels: a)Young's modulus; b) Yield strength; c) Poisson's ratio; d) Heat capacity; e)Thermal expansion; f) Thermal conductivity.

Table 1 Material parameters for M50 and 4340 steel in ambient temperature.

Symbol	Description	M50	4340	Units

Just Accepted

	ρ	Density	7980	7830	kg/m^3
	E	Young's modulus	210	205	GPa
	ν	Poisson's ratio	0.29	0.28	-
Mechanical	σ_{y0}	Initial yield strength	2800	850	MPa
	σ_{sa}	Isotropic hardening saturation value	800	150	MPa
	b	Isotropic hardening rate	6.68	5.0	-
	α_θ	Thermal expansion coefficient	11.5	11.2	K^{-1}
	ω_1	Softening rate	0.0085	0.0065	K^{-1}
	a_1	Fitting parameter	0.117	0.25	mm^{-1}
	a_2	Fitting parameter	0.119	0.05	mm^{-1}
Thermal	c_θ	Specific heat capacity	480	413	$J/(kg \cdot K)$
	k_0	Thermal conductivity	37.5	44.6	$W/(m \cdot K)$

Just Accepted

	η	Taylor-Quinney coefficient	0.9	0.9	-
	θ_0	Reference temperature	20	20	℃
	θ_m	Melt temperature	1500	1417	℃
Phase - field	$\mathcal{G}_c$	Critical strain energy release rate	14000	45000	J/m^2
	l_c	Length scale parameter	80	80	μm

3. Results

3.1. Dynamic response of the ring and cage at impact-sliding contact

Before presenting the detailed parametric results and microstructural damage evaluations in this section, it should be noted that the rigorous validity and predictive capability of the proposed thermo-elasto-plastic phase-field framework have been verified against theoretical analytical limits, the details of which are discussed in Section 4.4. Figure 5 illustrates the transient evolution of the maximum contact pressure at the impact-sliding interface under varying sliding velocities (V_i=0.6 *m/s,* μ=0.5) and impact velocities (V_s=75 *m/s,* μ=0.5). It should be emphasized that while the friction coefficient under normal, well-lubricated aero-engine operating conditions typically remains below 0.1, this study explicitly targets extreme failure modes. Consequently, a high friction coefficient of μ = 0.5 is prescribed in the simulations. This value acts as an extreme boundary condition, representing severe transient anomalies such as boundary lubrication breakdown, momentary oil starvation, or metal-to-metal galling induced by cage instability. The red block in Fig. 5 denotes the shifts in peak stress timing and the corresponding stress attenuation rates, highlighting the sensitivity of the contact evolution to these high-speed kinematic parameters. It shows that the maximum contact pressure

Just Accepted

increases to a peak value, then decreases to zero during the impact-sliding process. As Fig. 5(a) shows, an increase in the initial sliding velocity V_s leads to a significant rise in the peak P_{max}. The occurrence of the peak P_{max} is delayed, and the total contact duration is reduced as the P_{max} decreases to zero more rapidly as the V_s increases. As the Fig. 5(b) shows, the trend observed of P_{max} for V_i increment is similar to that of the case for V_s. However, increasing V_i shifts the peak stress timing earlier and results in a more rapid decline to zero, indicating a shorter contact duration.

Figure 6 illustrates the transient temperature evolution of the ring and cage during the impact-sliding contact process under various initial sliding velocities (V_i=0.6 *m/s,* μ=0.5) and impact velocities (V_s=75 *m/s,* μ=0.5). It shows a temperature increase as the initial sliding velocities and impact velocities increase. The rapid temperature rise is primarily attributed to intense frictional heat generation at the contact interface and dissipation of plastic work within the localized deformation zone. As Fig. 6(a) and 6(b) show, the initial sliding velocity significantly influences the thermal response. With an increase in V_s, the peak temperatures for both the ring and the cage increase dramatically. The cage reaches a higher peak temperature because heat is concentrated in a relatively fixed region of its surface, while the contact sweeps along the ring. At the highest sliding velocities in Fig. 6(b), the calculated cage temperature exceeds the melting point in Table 1. These values lie outside the solid-state model's physical range, as explained in Section 2.6. This range depends on the loading conditions, friction coefficient and heat partition, not on sliding velocity alone. The timing of the temperature peak also varies with sliding velocity. In Figs. 6(c) and 6(d), higher impact velocities give higher peak temperatures in both bodies.

Just Accepted

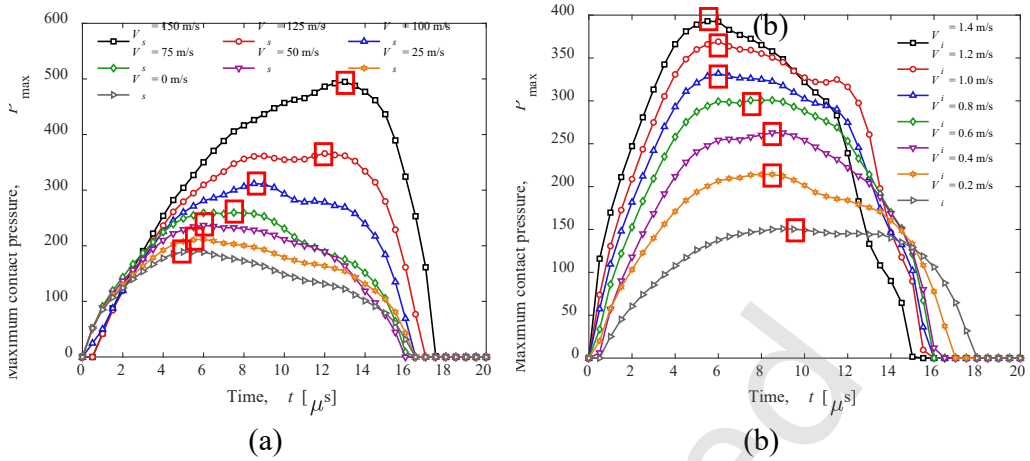


Fig. 5. Dynamic response of the maximum contact pressure during the impact-sliding process under different initial dynamic status: a) initial sliding velocity V_s (V_i=0.6 *m/s*, μ=0.5); b) initial impact velocity V_i (V_s=75 *m/s*, μ=0.5).

Just Accepted

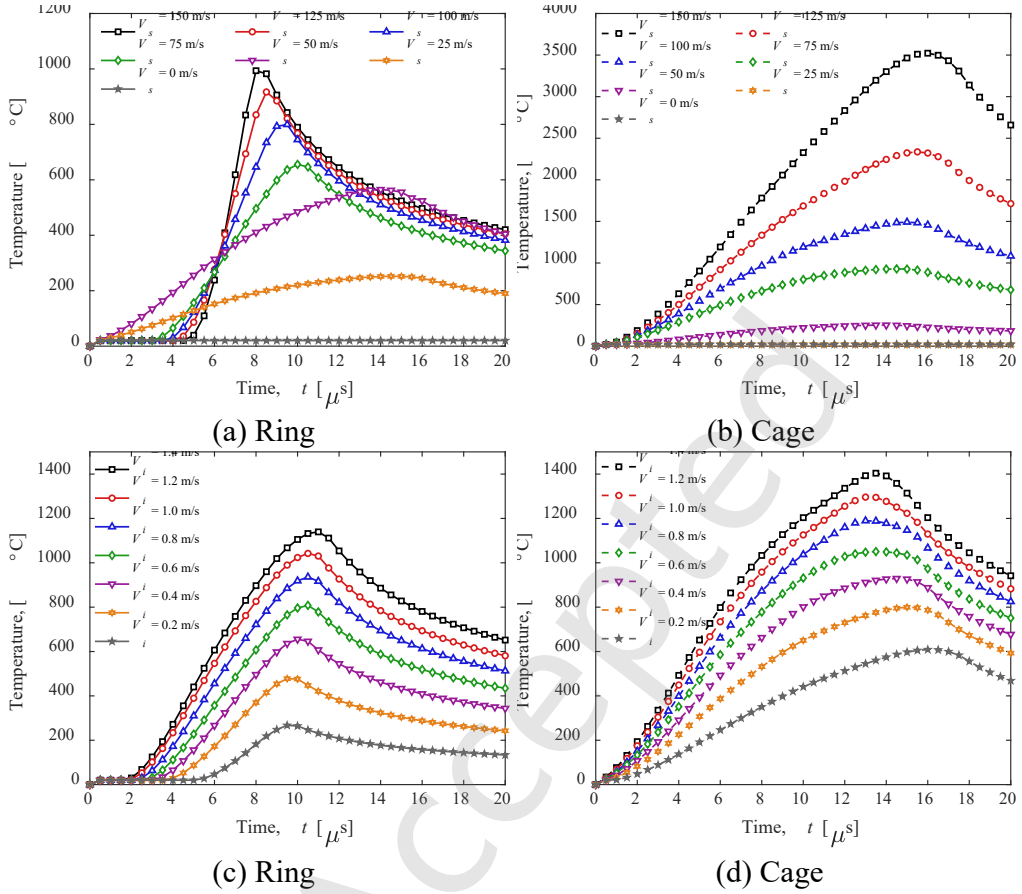


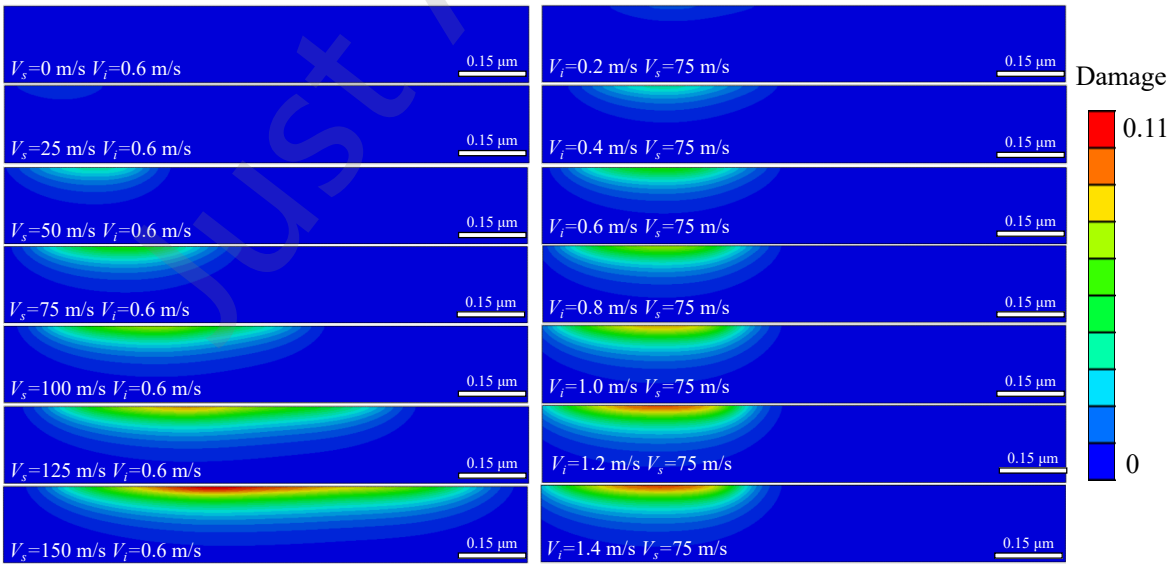
Fig. 6. Transient temperature evolution of the ring and cage under varying initial dynamic conditions: a) initial sliding velocity for ring; b) initial sliding velocity for cage; c) initial impact velocity for ring; d) initial impact velocity for cage.

3.2. Phase-field damage distribution and morphology

To visually elucidate the incipient damage accumulation patterns and confirm the competitive degradation mechanism between the interacting components, the cross-sectional spatial contours of the phase-field damage parameter at the end of the transient impact-sliding process are extracted. Fig. 7 and Fig. 8 show the damage distribution for the M50 steel ring and the 4340 steel cage under varying initial sliding velocities and impact velocities, respectively. Both the M50 steel ring and the 4340 steel cage exhibit a characteristic surface-originated profile. As shown in Fig. 7(a), as the initial

Just Accepted

sliding velocities increase, the damaged area of the M50 steel ring is stretched and dragged along the sliding direction. Kinematically, this elongation occurs because the dynamic interaction acts as a moving load and moving heat source relative to the ring surface; higher sliding velocities inherently extend the physical sweeping trajectory of the contact patch over the given transient duration. This morphological variation in the damaged area is a classic manifestation of early-stage damage precursor of friction-induced scuffing, driven by localized tangential shear traction and extremely high flash temperatures. As shown in Fig. 7(b), as the initial impact velocities increase, the damage increases and the damaged area of the M50 steel ring expands beneath the contact area. Similarly, for the 4340 steel cage shown in Fig. 8, as the initial sliding and impact velocities increase, damage increases, and the damaged area expands beneath the contact area. The cage's kinematics govern this response. The impact-sliding interaction behaves as a stationary contact patch relative to the cage body. Consequently, the entire thermo-mechanical energy flux is continuously pumped into the unchanging localized area. This concentrated, stationary accumulation of energy forces damage to propagate volumetrically and deeply beneath the contact interface, rather than spreading laterally.



(a) varying initial sliding velocity (b) varying initial impact velocity

Just Accepted

Fig. 7. Phase-field damage distribution of the ring under different initial dynamic status: a) initial sliding velocity V_s (V_i=0.6 *m/s,* μ=0.5); b) initial impact velocity V_i (V_s=75 *m/s,* μ=0.5).

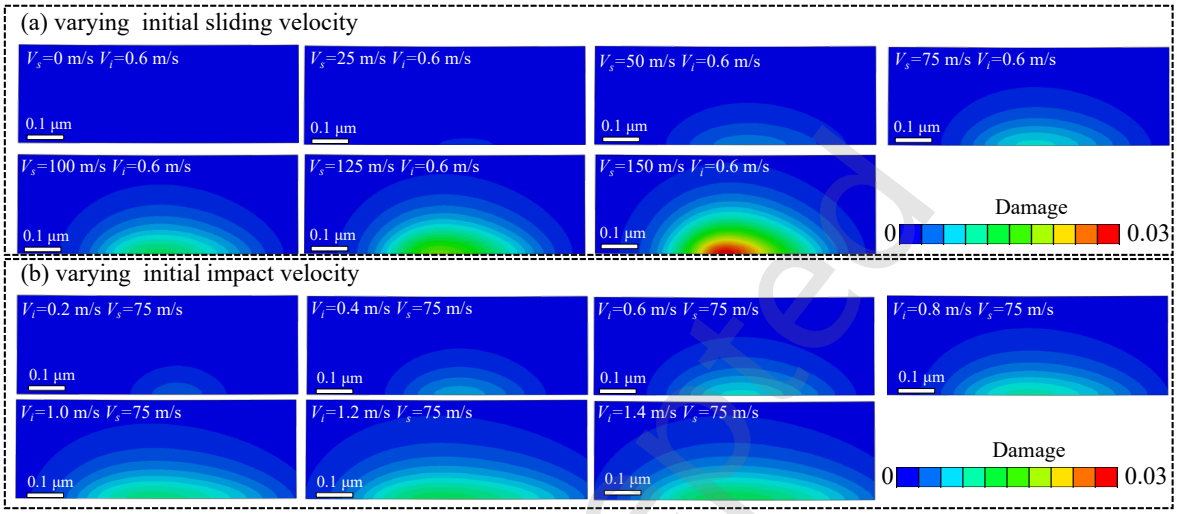


Fig. 8. Phase-field damage distribution of the cage under different initial dynamic status: a) initial sliding velocity V_s (V_i=0.6 *m/s,* μ=0.5); b) initial impact velocity V_i (V_s=75 *m/s,* μ=0.5).

3.3. Energy dissipation and damage evolution with different interfacial friction coefficients

Interfacial friction directly dictates tangential shear traction, thereby profoundly altering the surface heat generation and the subsequent partitioning of elasto-plastic energy densities, which ultimately govern the phase-field damage evolution. Therefore, this section performed phase-field damage simulations with varying friction coefficients from 0.01 to 0.5, using an initial sliding velocity of 75 m/s and an initial impact velocity of 0.6 m/s. Friction coefficients from 0.01 to 0.5 include elastohydrodynamic lubrication, mixed lubrication, and severe boundary lubrication or dry contact conditions. The friction coefficient serves as a powerful global amplifier of thermo-mechanical energy conversion at the impact-sliding interface. As shown in Fig. 9, an increase in the friction coefficient triggers a corresponding yet highly nonlinear surge in both thermal and mechanical

Just Accepted

responses. As shown in Fig. 9(b) and 9(f), the frictional work drastically elevates the localized flash temperatures. Compared with the M50 steel ring, the 4340 steel cage exhibits a significantly higher thermal sensitivity. The elastic strain energy density of the M50 steel ring and the 4340 steel cage are shown in Fig. 9(c) and 9(g). They show that the elastic strain energy density is a reversible quantity associated with the loading and unloading contact process. The elastic strain energy density of the M50 steel is significantly higher than that of the 4340 steel cage. This is because M50 steel has a significantly higher yield strength than 4340 steel. In contrast to the reversible elastic strain energy, the plastic energy density is irreversible, as shown in Fig. 9(d) and 9(h). The plastic energy density increases and then reaches a plateau for both the M50 steel ring and the 4340 steel cage at high friction coefficients. The high-hardness M50 ring strongly resists plastic yielding at lower friction levels. However, once the friction condition reaches a high value, such as 0.5, the plastic energy exhibits a sudden, exponential leap from near zero to over 9 MJ/m^3. This abrupt transition signifies a localized constitutive collapse, in which severe frictional heating outpaces thermal diffusion, triggering thermal softening that suddenly overrides the material's yield strength.

The distinct energy partitioning directly governs the ultimate structural degradation, as depicted in the damage evolution curves shown in Fig. 9(a) and 9(b). The phase-field damage nucleates rapidly after a brief incubation period and subsequently plateaus as the contact decouples. Driven by the immense combined accumulation of elastic driving forces and abrupt plastic dissipation under high friction, the final damage variable of the M50 ring is numerically higher than that of the cage under this specific heat-partitioning constraint. These results compellingly confirm that excessive tangential friction is the primary thermodynamic catalyst driving accelerated localized surface damage initiation and phase-field degradation.

Just Accepted

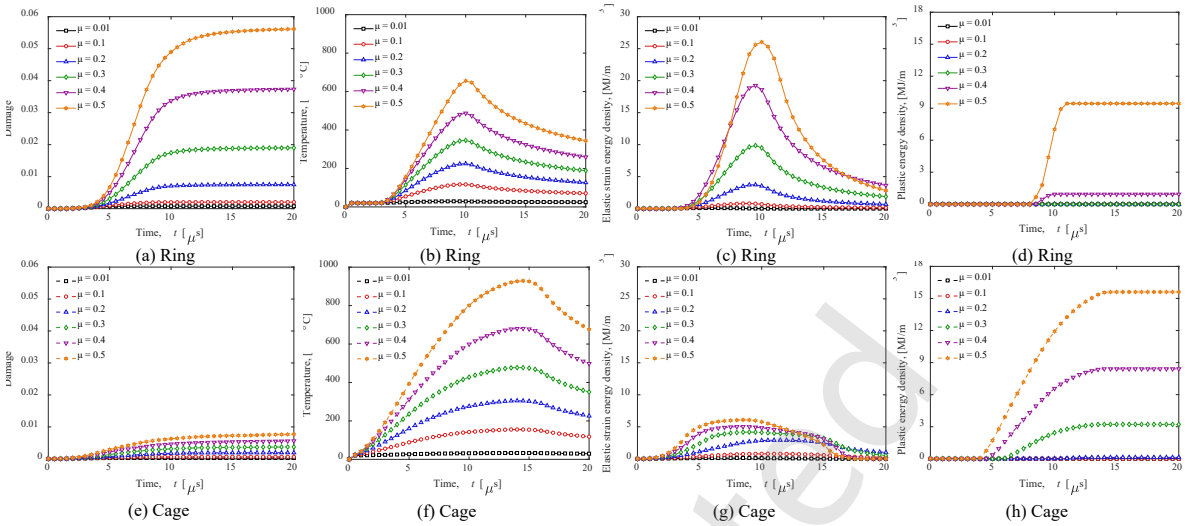


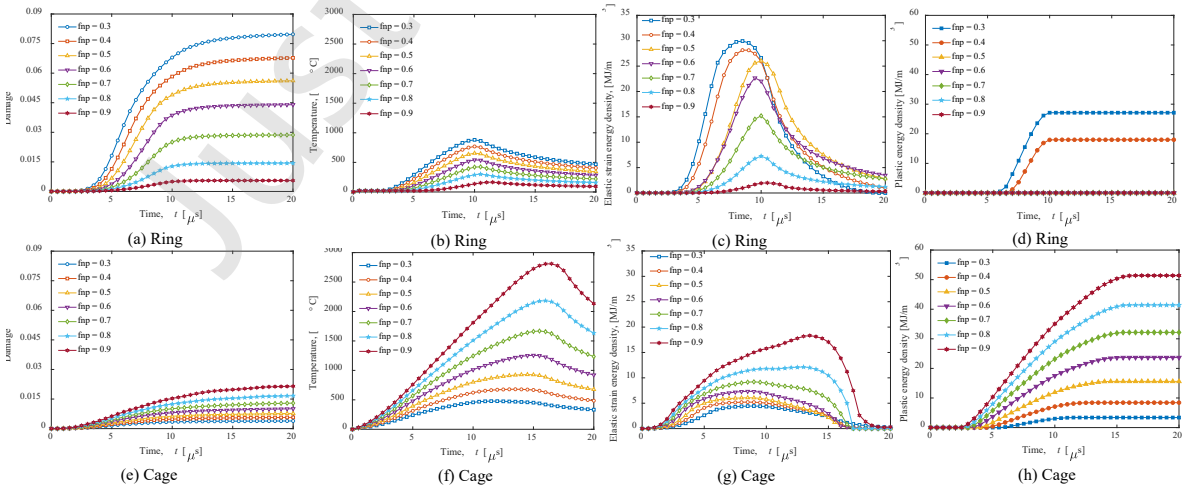
Fig. 9 Dynamic thermo-mechanical responses and phase-field damage accumulation of the interacting M50 steel ring and 4340 steel cage with different interfacial friction coefficient (V_s=75 *m/s,* V_i=0.6 *m/s*): a) damage of ring; b) temperature of ring; c) elastic strain energy density of ring; d) plastic energy density of ring; e) damage of cage; f) temperature of cage; g) elastic strain energy density of cage; h) plastic energy density of cage.

3.4. Energy dissipation and damage evolution with different thermal partition coefficients

The thermal partition coefficient (fnp) fundamentally governs the allocation of frictionally generated heat across the contact interface. The actual magnitude of fnp is highly sensitive to sophisticated interfacial engineering interventions, such as the application of thermal barrier coatings, high-conductivity solid lubricant films, or micro-texturing. Fundamentally, heat partitioning is governed by the ratio of the surface thermal effusivities ($e = \sqrt{k\rho c}$, where k is thermal conductivity, ρ is density, and c is specific heat of the contacting bodies [43]. In this computational framework, the M50 steel ring is designated as the primary contact surface, while the 4340 steel cage acts as the secondary surface. The value of fnp represents the fraction of the total interfacial frictional heat channeled into the secondary surface, with a default baseline of 0.5. In this study, fnp is treated as a parameterized

Just Accepted

constant across individual simulations to model the macroscopic thermal effects of engineered surface modifications, such as thermal barrier coatings, solid lubricant films, and micro-texturing, which modify localized thermal resistance and direct the interfacial heat flux distribution. Consequently, this study investigates the variation of fnp to explore how such engineered heat partitioning dictates the competitive degradation and thermal-mechanical failure mechanisms between the interacting components. To quantitatively evaluate the influence of frictional heat allocation at the contact interface, the transient evolutions of local temperature, elasto-plastic energy densities, and phase-field damage are extracted for thermal partition coefficients ranging from 0.3 to 0.9. As shown in Fig. 10(b) and 10(f), increasing the prescribed heat partition coefficient raises the cage temperature and lowers the ring temperature. The model also gives greater plastic dissipation and damage in the cage, with smaller values in the ring. Some cage temperatures in Fig. 10(f) exceed the melting point even at V_s = 75 m/s. The stresses and damage in those cases depend on material properties extrapolated beyond their supported range. The results show how heat allocation affects the calculated damage in each body; they do not establish a safe heat-partition threshold for bearing design or describe damage after melting.



Just Accepted

Fig. 10 Dynamic thermo-mechanical responses and phase-field damage accumulation of the interacting M50 steel ring and 4340 steel cage with different thermal partition coefficient (V_s=75 *m/s,* V_i=0.6 *m/s*): a) damage of ring; b) temperature of ring; c) elastic strain energy density of ring; d) plastic energy density of ring; e) damage of cage; f) temperature of cage; g) elastic strain energy density of cage; h) plastic energy density of cage.

4. Discussion

4.1 Effect of initial dynamic transient condition on damage behavior

To elucidate the effects of the initial dynamic transient condition on the damage behavior for both the M50 steel ring and the 4340 steel cage, the maximum damage on the contact surface for the ring and cage varying initial sliding velocity and impact velocity are shown in Fig. 11. For both ring and cage, the gradient of damage growth with respect to the impact velocity becomes steeper at higher slip velocity. This synergistic aggravation fundamentally stems from the dual-driven nature of the localized constitutive collapse. The initial impact velocity serves as the primary mechanical driving force. This enhances the contact pressure and induces the localized elastic strain energy. Simultaneously, the initial sliding velocity acts as the thermal driving force, generating intense interfacial frictional heat and triggering extreme thermal softening. When the impact velocity increases to a severe value, the high contact pressure significantly lowers the critical threshold required for thermal yielding. Consequently, severe sliding readily overwhelms the compromised strain-hardening capacity of the material, precipitating catastrophic thermoplastic flow and accelerated phase-field damage accumulation. Furthermore, the absolute damage magnitudes plotted in Fig. 11 confirm that the M50 steel ring is more likely to be damaged than the 4340 steel cage under impact-sliding contact conditions. Despite the cage experiencing damage growth, the maximum damage severity in the ring is nearly an order of magnitude higher than that in the cage. This indicates

Just Accepted

that the M50 is highly susceptible to these combined thermal-mechanical conditions and suffers severe localized surface damage without deliberate dynamic heat-partitioning interventions.

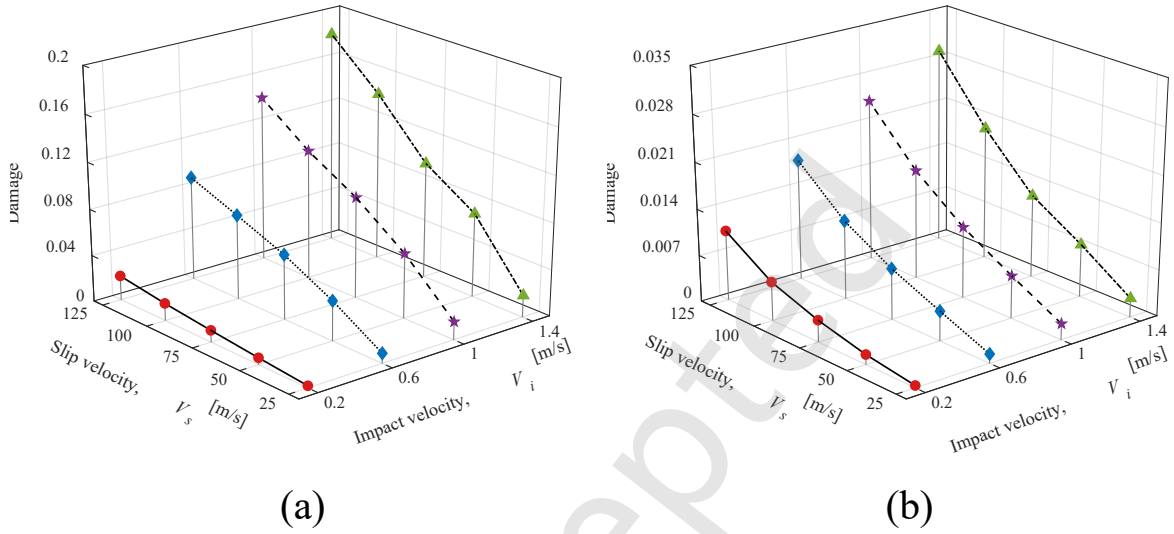


Fig. 11 Effects of initial sliding velocity and impact velocity on the damage of the component: a) M50 steel ring; b) 4340 steel cage.

4.2 Effect of heat partition coefficient on the damage behavior

The heat partition coefficient governs the allocation of frictionally generated heat across the contact interface. To systematically decouple the synergistic effects of contact kinematics and interfacial heat partitioning on the M50 steel ring and the 4340 steel cage, a damage transition phase diagram is constructed, as shown in Fig. 12. While fnp is prescribed as a constant input in each simulation, the resulting phase boundary reflects an intrinsic nonlinear constitutive competition between the two materials rather than a trivial proportional scaling of thermal input. The contour map illustrates the ultimate phase-field damage differential, mapped across a broad spectrum of initial sliding velocity and thermal partition coefficients. The solid black line indicates the critical interfacial failure transition boundary. The domain beyond the solid black line, shown in blue, indicates that the damage in the 4340 steel cage is more severe than that in the M50 steel ring, a regime called the cage-

Just Accepted

dominant regime. Conversely, the domain below the solid black line, shown in red, indicates that the damage to the M50 steel ring is more severe than that to the 4340 steel cage, a regime called the ring-dominant regime. In the cage-dominant regime, the relatively tougher 4340 steel cage absorbs extreme frictional heat through extensive thermoplastic yielding and volumetric damage, thereby structurally shielding the ring. A critical micro-mechanical insight revealed by Fig. 11 is the negative slope of the transition boundary. At a moderate slip velocity (V_s = 50 m/s), a relatively high partition coefficient (fnp = 0.78) is required to channel sufficient heat into the cage to trigger its sacrificial thermal softening. However, under extreme hyper-velocity sliding (V_s = 125 m/s), the total rate of friction-induced adiabatic heating is so immense that a noticeably lower partition threshold (fnp = 0.72) is sufficient to precipitate the constitutive collapse of the 4340 steel cage. This indicates that as the kinetic energy input escalates, the system's reliance on asymmetric heat partitioning to protect the ring is paradoxically alleviated due to the sheer magnitude of the total thermal flux available to soften the cage. This diagram provides a physics-based criterion for the advanced design of high-speed aeroengine bearings. To prevent failure of the primary load-bearing component, the M50 ring under transient impact-sliding conditions, the tribological system must be deliberately engineered to operate within the cage-dominant zone. Consequently, surface engineering interventions—such as applying localized thermal barrier coatings, tailoring surface texturing, or modifying the specific heat capacity of the interacting surfaces—should be strategically implemented to artificially elevate the heat partition coefficient above this critical transition boundary. By manipulating the dynamic heat flux, the inevitable destructive energy can be purposefully guided into the ductile cage, ensuring the survivability of the core bearing assembly.

It should be noted that the specific transition boundary presented in Fig. 12 is valid for the current prescribed kinetic conditions (V_i = 0.6 m/s, $\mu = 0.5$). The topological morphology of this boundary is highly sensitive to variations in these parameters. On the one hand, an increase in the friction

Just Accepted

coefficient would exponentially escalate the total frictional heat flux. Analogous to the effect of increasing sliding velocity, this would shift the entire transition boundary downwards, indicating that a lower fnp threshold is required to trigger the thermal collapse of the cage. On the other hand, an increase in the normal impact velocity drastically amplifies the localized mechanical contact pressure. Because the high-hardness M50 ring is inherently vulnerable to stress-concentrated elastic spalling, a higher mechanical load makes the ring fail more prematurely. Consequently, protecting the M50 ring at higher impact velocities demands an enhanced sacrificial buffering effect, which would shift the transition boundary upward, thereby requiring a more aggressive thermal partitioning (higher fnp) into the cage.

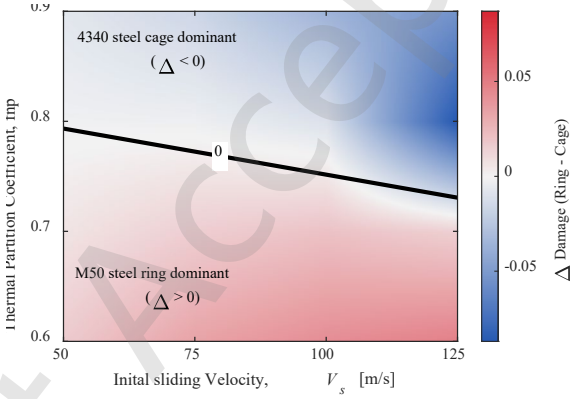


Fig. 12 Effects of initial sliding velocity and heat partition coefficient on the damage competition boundary between the M50 steel ring and 4340 steel cage.

4.3 Competitive mechanism of damage between M50 and 4320 steel

The failure boundary and kinematic synergistic effects discussed in Sections 4.1 and 4.2 originate from the fundamental constitutive discrepancy between the interacting materials. The competitive mechanism of damage under impact-sliding contact is not only a simultaneous degradation of the two surfaces but also a complex, thermodynamically governed elasto-plastic and thermal softening response. The M50 steel has an ultra-high initial yield strength, which gives it good rolling contact

Just Accepted

fatigue resistance. However, the high yield strength of M50 steel makes it highly vulnerable to sudden kinetic-energy impacts. Consequently, M50 cannot efficiently dissipate impact energy through localized plastic flow. Instead, the intense mechanical work is abruptly converted into highly concentrated tensile elastic strain energy confined within a microscopically thin superficial layer. Once this concentrated elastic energy exceeds the critical fracture toughness, it triggers intense, localized superficial damage accumulation, serving as the primary nucleation precursor for subsequent spalling. Thus, the failure of the M50 ring is predominantly mechanically driven and dominated by elasticity. Conversely, the 4340 steel cage has superior ductility and a high sensitivity to thermal softening. The 4340 steel accommodates the impact kinetic energy through massive, volumetric thermoplastic flow. However, under uniform or natural heat partitioning, insufficient thermal energy reaches the cage to trigger its massive thermoplastic yielding, rendering its energy-absorption potential largely dormant. This explains why the unyielding M50 ring inevitably incurs severe localized damage and degradation under default scenarios. To shield the M50 ring, the system must be deliberately engineered to operate within the cage-dominant regime discussed in Section 4.2.

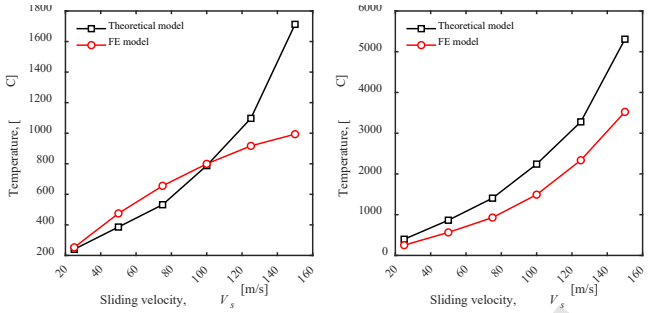
4.4 Verification

To validate the proposed explicit thermomechanical framework, the maximum interfacial temperatures predicted by the FE model in this study are compared with classical analytical solutions. The Tian-Kennedy model [44] and the Carslaw-Jaeger integral model [45] are selected as the theoretical models for comparison with the moving M50 steel ring and the stationary 4340 steel cage, respectively. The comparison results are shown in Fig. 13. For the M50 ring, the FE temperature rises less steeply at high sliding velocities than the analytical estimate. For the 4340 cage, both curves rise with velocity, but the analytical values remain higher. The differences in trend and magnitude mean that the comparison does not quantitatively verify the model over the full velocity range. The FE formulation includes temperature-dependent properties and coupled changes in contact, plasticity and

Just Accepted

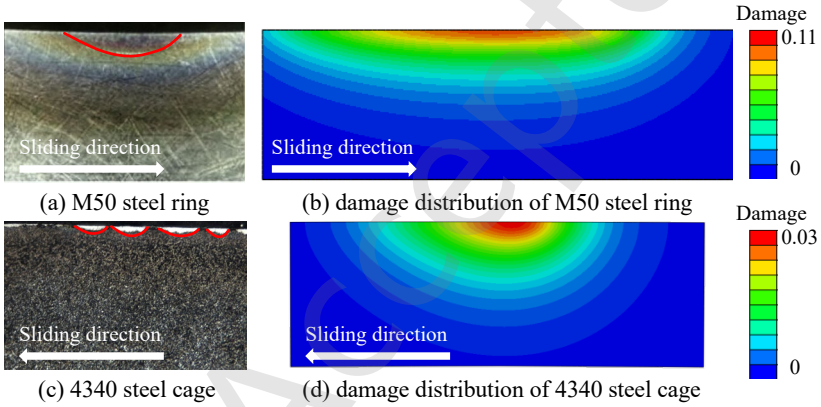
damage. These features, together with differences in the heat-source history, may contribute to the discrepancies. Their separate effects cannot be identified from Fig. 13. In particular, the elongated damage patterns in Fig. 7(a) do not measure contact width or heat-source exposure time. They cannot establish contact-area redistribution as the cause of the ring's temperature trend. Figure 13(b) also contains temperatures above the melting point in Table 1. These are extrapolations of the solid-state model, which does not include melting or molten-material behaviour. Comparing them with analytical estimates does not establish their physical validity. The limitations described in Section 2.6 apply to these results. Furthermore, damage distribution validation of the M50 ring is shown in Fig. 14(a) and (b), comparing the simulated damage contour with an experimental micrograph of the contact cross-section from Wang et al. [15]. The experimental observation reveals a distinct semi-elliptical heat-affected zone extending into the substrate. Remarkably, the FE model perfectly replicates this semi-elliptical spatial gradient, accurately capturing the depth and lateral diffusion of the thermomechanical energy. In contrast, a qualitative morphological comparison of the 4340 steel cage is illustrated in Fig. 14(c) and (d). The experimental micrograph was obtained from a post-failure 4340 steel cage of an aero-engine mainshaft cylindrical roller bearing following an extreme oil-starvation (lubricant cut-off) test conducted in our laboratory. The experimental micrograph displays discrete, highly localized, pocket-like damage patches rather than a continuous strip. This distinct morphological feature stems from the specific kinematic nature of the cage: during each individual collision, the loaded area remains stationary relative to the cage surface, while successive dynamic impacts occur at slightly shifted adjacent locations. Results in Fig. 14(d) precisely mirror the foundational mechanism of this localized phenomenon, demonstrating a concentrated, deep spherical energy diffusion profile without horizontal elongation. This morphological consistency across both components, combined with the quantitative numerical validation, verifies that the proposed framework authentically captures the true subsurface energy dissipation and kinematic-driven degradation mechanisms.

Just Accepted



(a) M50 steel ring (b) 4340 steel cage

Fig. 13 Temperature validation of the FE model against theoretical solutions: a) M50 steel ring; b) 4340 steel cage.



(a) M50 steel ring (b) damage distribution of M50 steel ring

(c) 4340 steel cage (d) damage distribution of 4340 steel cage

Fig. 14 Validation of the damage distribution: a) experimental result of the M50 steel ring; b) numerical result of the M50 steel ring (V_s=75 *m/s,* V_i=1.4*m/s,* fnp=0.6); c) experimental result of the 4340 steel cage; d) numerical result of the 4340 steel cage (V_s=125 *m/s,* V_i=0.6*m/s,* fnp=0.6).

5. Conclusions

In this study, a fully coupled, dual-body explicit thermo-elasto-plastic phase-field framework was developed to investigate the transient impact-sliding damage behavior at the interface of an M50 steel ring and an AISI 4340 steel cage. The explicit pseudo-dynamic architecture successfully overcame the convergence limitations of traditional implicit solvers, enabling a high-fidelity

Just Accepted

exploration of the dual-body competitive degradation mechanisms. The main conclusions are drawn as follows:

1) Tangential sliding serves as a thermal driver, causing pronounced elongation of horizontal superficial damage in the M50 ring. Normal impact serves as a mechanical driver, governing the vertical penetration of subsurface fatigue in the 4340 cage. Their synergistic interaction significantly lowers the thermal yielding threshold, accelerating localized damage accumulation.

2) Interfacial friction non-linearly amplifies global energy. Under extreme friction, intense adiabatic heating breaches the Fermi-Dirac thermal softening threshold, triggering an abrupt localized constitutive collapse. This exponentially increases irreversible plastic dissipation and accelerates damage.

3) A failure transition boundary governed by the interfacial thermal partition coefficient is identified. Channeling frictional heat into the tougher 4340 cage forcefully activates its extreme thermoplastic yielding. Within this regime, the cage serves as a thermodynamic sacrificial layer, absorbing destructive thermal-mechanical fluxes to physically shield the core M50 ring from severe localized structural degradation.

4) By transforming the quasi-static phase-field formulation into a pseudo-dynamic wave-propagation problem, the architecture entirely circumvents global stiffness-matrix singularities. Validated against analytical theories and experiments, it intrinsically captures geometric adaptive mechanisms, demonstrating that thermal-induced contact area expansion effectively mitigates peak flash temperatures under extreme conditions.

Just Accepted

Acknowledgments

This work was supported by the National Natural Science Foundation of China (No. 52405185).

Author Contributions

Conflict of Interest

The authors declare there is no conflict of interest in this paper.

Under Peer Review

References

[1] Bhadeshia H K D H. Steels for bearings. *Progress in Materials Science* 57(2): 268–435 (2012)
[2] Yu X F, Zheng D Y, Yang X F, Wang S Y, An M, Yan G B, Xia Y Z, Xing F. Effect of carbide precipitation behavior at high temperatures on microstructure and mechanical properties of M50 steel. *Journal of Materials Research and Technology* 18: 1155–1165 (2022)
[3] Nygaard J R, Rawson M, Danson P, Bhadeshia H. Bearing steel microstructures after aircraft gas turbine engine service. *Materials Science and Technology* 30(15): 1911–1918 (2014)
[4] Forster N H, Trivedi H K. Rolling Contact Testing of Vapor Phase Lubricants–-Part I: Material Evaluation. *Tribology transactions* 40(3): 421–428 (1997)
[5] Tomaz Í do V, Martins M C, Costa H R M, Bastos I N, Fonseca M C. Influence of residual stress on the sliding wear of AISI 4340 steel. *Matéria (Rio de Janeiro)* 25(2): e-12618 (2020)
[6] Ramprasad M, Mayuram M M. Some studies on scuffing performance of surface treated AISI 4340 steels. *J. Trib.* 125(1): 181–186 (2003)
[7] Lee W-S, Su T-T. Mechanical properties and microstructural features of AISI 4340 high-strength alloy steel under quenched and tempered conditions. *Journal of materials processing technology* 87(1–3): 198–206 (1999)
[8] Han Y, Wang L, Lin F, Wu J, Liu Y, Cao Y, Liu P, Li Z, Zhang D, Zhang X. Evolution Characteristics and Failure Mechanism of Aero-Engine Mainshaft Bearings under Oil Cut-off Conditions. *Tribology International* 111391 (2025)
[9] Russell T, Sadeghi F. The effects of lubricant starvation on ball bearing cage pocket friction. *Tribology International* 173: 107630 (2022)
[10] Messaadi M, Kapsa P. Wear behavior of high chromium sintered steel under dynamic impact-sliding: Effect of temperature. *Tribology International* 100: 380–387 (2016)
[11] Ghaisas N, Wassgren C R, Sadeghi F. Cage instabilities in cylindrical roller bearings. *J. Trib.* 126(4): 681–689 (2004)
[12] Tu W, Liang J, Yu W, Shi Z, Liu C. Motion stability analysis of cage of rolling bearing under the variable-speed condition. *Nonlinear Dynamics* 111(12): 11045–11063 (2023)
[13] Nogi T, Maniwa K, Matsuoka N. A Dynamic Analysis of Cage Instability in Ball Bearings. 2017.
[14] Ma S, Zhang X, Yan K, Zhu Y, Hong J. A study on bearing dynamic features under the condition of multiball–cage collision. *Lubricants* 10(1): 9 (2022)
[15] Wang C, Zhang C, Gu L, Bi M, Hou P, Zheng D, Wang L. Analysis on surface damage of M50 steel at impact-sliding contacts. *Tribology International* 150 (2020)
[16] Zhu D, Jane Wang Q. Elastohydrodynamic lubrication: a gateway to interfacial mechanics—review and prospect (2011)

[17] Kennedy Jr F E. Thermal and thermomechanical effects in dry sliding. *Wear* 100(1–3): 453–476 (1984)
[18] Wu C-Y, Li L-Y, Thornton C. Energy dissipation during normal impact of elastic and elastic–plastic spheres. *International Journal of Impact Engineering* 32(1–4): 593–604 (2005)
[19] Müller P, Böttcher R, Russell A, Trüe M, Aman S, Tomas J. Contact time at impact of spheres on large thin plates. *Advanced Powder Technology* 27(4): 1233–1243 (2016)
[20] Gheadnia H, Cermik O, Marghitu D B. Experimental and theoretical analysis of the elasto-plastic oblique impact of a rod with a flat. *International Journal of Impact Engineering* 86: 307–317 (2015)
[21] Li J C, Chen X W. Theoretical analysis of projectile-target interface defeat and transition to penetration by long rods due to oblique impacts of ceramic targets. *International Journal of Impact Engineering* 106: 53–63 (2017)
[22] Dambakizi F, Le Tallec P, Perlat J P. A local thermomechanical model of friction for computing structures under extreme loading conditions. *International journal for numerical methods in engineering* 89(5): 561–583 (2012)
[23] Dambakizi F, Le Tallec P, Perlat J-P. Multiscale thermomechanical modeling of shock-driven dry friction in hydrodynamics. *Computer methods in applied mechanics and engineering* 198(21–26): 1701–1715 (2009)
[24] Lemaitre J. A continuous damage mechanics model for ductile fracture (1985)
[25] Chaboche J-L. Continuum damage mechanics: Part I—General concepts (1988)
[26] Gurson A L. Continuum theory of ductile rupture by void nucleation and growth: Part I—Yield criteria and flow rules for porous ductile media (1977)
[27] Johnson G R, Cook W H. Fracture characteristics of three metals subjected to various strains, strain rates, temperatures and pressures. *Engineering fracture mechanics* 21(1): 31–48 (1985)
[28] Bao Y, Wierzbicki T. On fracture locus in the equivalent strain and stress triaxiality space. *International journal of mechanical sciences* 46(1): 81–98 (2004)
[29] Xue L. Damage accumulation and fracture initiation in uncracked ductile solids subject to triaxial loading. *International journal of solids and structures* 44(16): 5163–5181 (2007)
[30] Miehe C, Hofacker M, Welschinger F. A phase field model for rate-independent crack propagation: Robust algorithmic implementation based on operator splits. *Computer Methods in Applied Mechanics and Engineering* 199(45–48): 2765–2778 (2010)
[31] Wang C, Aldakheel F, Zhang C, Gu L, Wriggers P. Shear instability of high-speed bearing at cyclic impact-sliding contacts Simulation and experimental testing of the collision behaviour of ships with double hulls filled with particles View project Virtual elements for problems undergoing finite strains View project Shear instability of high-speed bearing at cyclic impact-sliding contacts.
[32] Meyers M A, Andrade U R, Chokshi A H. The effect of grain size on the high-strain, high-strain-rate behavior of copper. *Metallurgical and materials transactions A* 26(11): 2881–2893 (1995)
[33] Zhang C, Peng B, Wang L, Ma X, Gu L. Thermal-induced surface damage of M50 steel at rolling-sliding contacts. *Wear* 420–421(November 2018): 116–122 (2019)
[34] Francfort G A, Marigo J-J. Revisiting brittle fracture as an energy minimization problem. *Journal of the Mechanics and Physics of Solids* 46(8): 1319–1342 (1998)
[35] Miehe C, Welschinger F, Hofacker M. Thermodynamically consistent phase-field models of fracture: Variational principles and multi-field FE implementations. *International journal for numerical methods in engineering* 83(10): 1273–1311 (2010)
[36] Ambati M, Gerasimov T, De Lorenzis L. Phase-field modeling of ductile fracture. *Computational Mechanics* 55(5): 1017–1040 (2015)

Just Accepted

[37] Aldakheel F, Wriggers P, Miehe C. A modified Gurson-type plasticity model at finite strains: formulation, numerical analysis and phase-field coupling. *Computational Mechanics* 62(4): 815–833 (2018)
[38] Taylor G I, Quinney H. The latent energy remaining in a metal after cold working. *Proceedings of the Royal Society of London. Series A, Containing Papers of a Mathematical and Physical Character* 143(849): 307–326 (1934)
[39] Carnevale E H, Lynnworth L C, Larson G S. Ultrasonic measurement of elastic moduli at elevated temperatures, using momentary contact. *The Journal of the Acoustical Society of America* 36(9): 1678–1684 (1964)
[40] Lee W-S, Yeh G-W. The plastic deformation behaviour of AISI 4340 alloy steel subjected to high temperature and high strain rate loading conditions. *Journal of materials processing technology* 71(2): 224–234 (1997)
[41] Fakir R, Barka N, Brousseau J. Case study of laser hardening process applied to 4340 steel cylindrical specimens using simulation and experimental validation. *Case Studies in Thermal Engineering* 11: 15–25 (2018)
[42] Hussain N, Qayyum F, Pasha R A, Shah M. Development of multi-physics numerical simulation model to investigate thermo-mechanical fatigue crack propagation in an autofrettaged gun barrel. *Defence Technology* 17(5): 1579–1591 (2021)
[43] Abdel-Aal H A. On the distribution of friction-induced heat in the dry sliding of metallic solid pairs. *International Communications in Heat and Mass Transfer* 24(7): 989–998 (1997)
[44] Tian X, Kennedy Jr F E. Maximum and average flash temperatures in sliding contacts (1994)
[45] Carlsaw H S, Jaeger J C. Conduction of heat in solids. *Clarendon, Oxford* (1959)



Wanjia LI is currently a research associate professor at Zhengzhou Advanced Research Institute, Harbin Institute of Technology, China, China. He obtained his Ph.D. degree in 2022 from Kyushu University. He was promoted to research associate professor in 2024 at Harbin Institute of Technology. He is a member of the Tribology Institute of Chinese Mechanical Engineering Society. His research areas include the theory of contact mechanism, rolling

Just Accepted

contact fatigue, fracture mechanics, damage mechanics, and hydrogen embrittlement of rolling bearing.



Tingjian WANG is a research associate professor at Zhengzhou Advanced Research Institute, Harbin Institute of Technology, China. He obtained his Ph.D. degree in 2016 from Harbin Institute of Technology. From 2013 to 2014, he was invited to visit the Northwestern University, USA, as a visiting scholar. He was promoted to assistant professor in 2016 and then to research associate professor in 2021 in Zhengzhou Research Institute, Harbin Institute of Technology Harbin Institute of Technology. He is a member of the Youth Working Committee of Tribology Institute of Chinese Mechanical Engineering Society. His interested research areas include contact mechanics and rolling bearing technology.

Just Accepted